Available online at www.sciencedirect.com
SCIENCE DIRECT
Ocean Modelling 13 (2006) 176–195
Ocean Modelling
www.elsevier.com/locate/ocemod

An OGCM with movable land–sea boundaries

Lie-Yauw Oey *

AOS Program, Princeton University, 205 Sayne Hall, Princeton, NJ 08544, USA

Received 23 June 2005; received in revised form 12 January 2006; accepted 16 January 2006
Available online 23 February 2006

Abstract

An ocean general circulation model (OGCM) with wetting and drying (WAD) capabilities removes the vertical-wall coastal assumption and allows simultaneous modeling of open-ocean currents and water run-up (and run-down) across movable land–sea boundaries. This paper implements and tests such a WAD scheme for the Princeton Ocean Model (POM) in its most general three-dimensional setting with stratification, bathymetry and forcing. The scheme can be easily exported to other OGCM's.

Keywords: Wetting and drying; Inundations; Ocean general circulation model (OGCM); Princeton Ocean Model (POM); Tides; Tsunamis; Estuarine outflows

1. Introduction

Open-sea models (i.e. OGCM's) are now routinely used to simulate eddies and jets as well as wind, river-buoyancy and tidal-driven flows; some OGCM's also have data assimilation capabilities for hindcast and forecast. Examples are: Chassignet et al. (2003), Dinniman and Klinck (2004), Ko et al. (2003), Marchesiello et al. (2003), Romanou et al. (2004), Sheng and Tang (2003), Smith et al. (2000), and our own model, Oey et al. (2003, 2004, 2005) and Fan et al. (2004). Our model is based on the Princeton Ocean Model (POM; Blumberg and Mellor, 1987) which, as do also virtually all open-sea models, assumes that the coast is a vertical wall, placed say at the 10 m isobath. Coastal boundaries constrain fluid flows and the land–sea interface also locally becomes important as one approaches the coast, where the vertical-wall assumption is clearly incorrect.

Estuarine and near-coast modelers must often deal with a land–sea boundary that is dynamically active: i.e. the land side can wet and the sea side can dry (Leendertse, 1970; Lynch and Gray, 1980; Stelling et al., 1986; Siden and Lynch, 1988; Flather and Hubbert, 1990; Falconer and Chen, 1991; Casulli and Cheng, 1992; Cheng et al., 1993; Hervouet and Van Haren, 1996; Balzano, 1998; Ji et al., 2001; Stelling and Duinmeijer, 2003; Oey, 2005; hereinafter, O2005). The physical reality of a dynamic coastal boundary is dramatically (and tragically) demonstrated during the Indian Ocean *tsunami* of 26 December 2004. Estuarine models that

* Tel.: +1 609 258 5971; fax: +1 609 258 2850.
E-mail address: lyo@princeton.edu

1463-5003/$ - see front matter
doi:10.1016/j.ocemod.2006.01.001

do treat *wetting and drying* (WAD) processes are generally detailed for localized (coastal) applications with less attention paid to open-sea simulations of, say, rings and oceanic jets such as the Loop Current or the Gulf Stream.

This paper implements WAD based on near-coast modelers' ideas (above) to the three-dimensional POM with general stratification and forcing. The upshot is a unified model that deals with both open-ocean and WAD physics. The numerical treatments detailed herein directly apply to many popular models that employ terrain-following sigma-coordinate on the *C*-grid, such as HYCOM (http://hycom.rsmas.miami.edu/; HYCOM uses sigma-coordinate on the shelf; in very shallow waters near the coast the coordinate switches back to *z*-coordinate; however, this may be a fixable artifice), NCOM (http://www7320.nrlssc.navy.mil/IAS-NFS_WWW/), and ROMS (http://marine.rutgers.edu/po/index.php?model=roms). With suitable changes, the techniques also apply to *z*-coordinate models; however, WAD processes in *z*-level are more restricted (Lin and Falconer, 1997). With regard to practical ocean forecast, this work may be useful to those who wish to design systems that are also relevant near the coast.

Section 2 discusses the WAD scheme. Section 3 tests the new code and Section 4 concludes the paper.

2. A wetting and drying scheme

Consider an ocean region R with land boundary ∂R (lands may be islands). The ocean state (sea-level, currents, density, etc.) as a function of space and time is to be simulated. OGCM's treat land boundaries as walls across which normal fluxes = 0; thus water depth $H \neq 0$ (10 m, say) at immediate grids seaward of ∂R. In codes, this zero-flux condition is often conveniently imposed by multiplying variables by a land mask FSM = 1 (0) at water (land) cells. O2005 removes this vertical-wall coastal constraint in POM using a simple WAD scheme. The scheme was tested on two-dimensional depth-averaged flows. I now extend the method to the full set of primitive equations in three dimensions with general baroclinicity and forcing.

2.1. Some definitions

Clear definitions of topography and height are necessary when discussing WAD (Fig. 1). Choose ∂R to be an absolute land boundary (ALB) across which water can never flood and FSM is set to 0. Given R, ∂R is

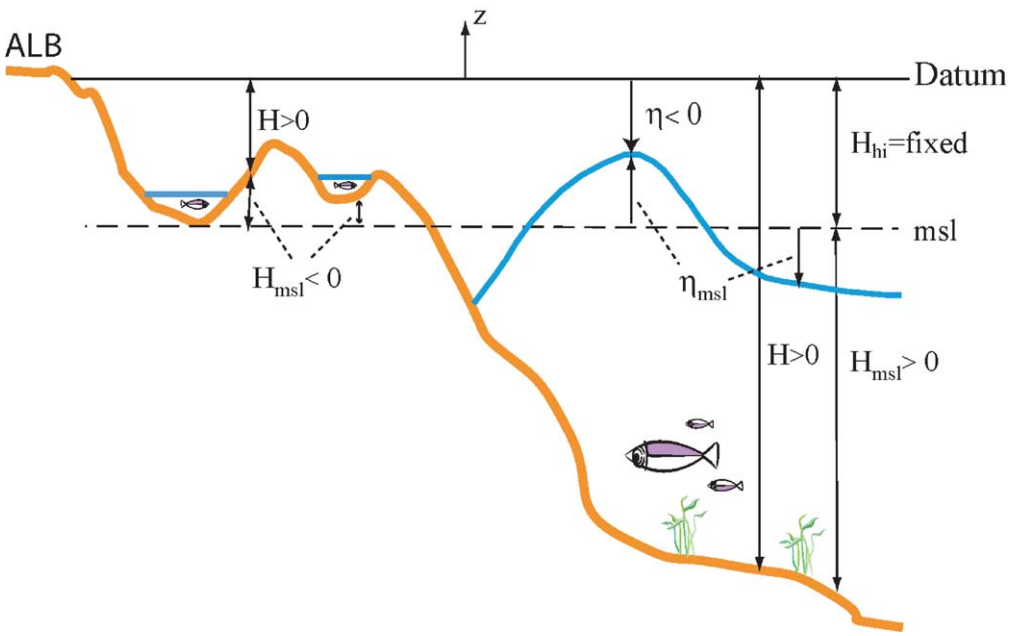

Fig. 1. Definitions of variables used in wetting and drying scheme. Acronyms ALB = absolute land boundary, msl = mean sea level.

easily chosen to be at some high ground taken as the datum $z = 0$. (We need not define ∂R for island(s) that can potentially be flooded). Bathymetric depth H is the non-negative (vertical) distance from the datum to the bottom topography, $H = H_{\rm msl} + H_{\rm hi}$, where $H_{\rm hi}$ is a constant height (>0) of the datum from the mean sea level (msl), and $H_{\rm msl}$ is height from the bottom to msl, positive (negative) if the bottom is below (above) the msl. Thus land, ∂R, is where $H_{\rm msl} = -H_{\rm hi}$, or $H = 0$. Then the ocean surface measured from the datum is $\eta(x,y,t) = -H_{\rm hi} + \eta_{\rm msl}(x,y,t) \leqslant 0$, where $\eta_{\rm msl}(x,y,t)$ defines deviation of surface from the msl. The total water depth is then

$$D = H + \eta(x,y,t) = H_{\rm msl} + \eta_{\rm msl}(x,y,t). \tag{2.1}$$

The second expression for D in (2.1) is the same as in the usual definition for ocean models. However, having defined $H(x,y)$ and $\eta(x,y,t)$, we will forgo using $H_{\rm msl}$ and $\eta_{\rm msl}$. It is easy to see (Fig. 1) that:

$$H \leqslant -\eta \quad \text{or} \quad D \leqslant 0 \qquad \text{if dry at any } (x,y,t) \tag{2.2}$$

and vice versa if wet.

There are two popular ways to treat WAD. One is to reconfigure boundary each time new dry and/or wet cells appear (e.g. Lynch and Gray, 1980). A mathematically less elegant but numerically easier way is to test for dry or wet cells at each time step using (2.2), then apply blocking conditions for fluxes at cells' interfaces (see Flather and Hubbert, 1990; Casulli and Cheng, 1992; Cheng et al., 1993; Ji et al., 2001 for comprehensive summaries). Here (and in O2005) we follow this second method. Although the followings are for POM, other models (HYCOM, NCOM and ROMS in particular) share similar structures: split-time stepping, *C*-grid, sigma-coordinate, etc. and the WAD treatments discussed herein may be imported.

2.2. External-mode conditions

POM uses an external/internal-mode time-splitting technique whereby depth-averaged equations (external) are time-stepped at $\Delta t_{\rm e}$ (usually) restricted by the fast surface gravity wave speed $c \approx (gD)^{1/2}$, where g is the acceleration due to gravity, through the Courant et al. (1928) or CFL condition for numerical stability. The three-dimensional internal-mode (or baroclinic) equations are time-stepped at $\Delta t_{\rm i}$ (usually $>>\Delta t_{\rm e}$) restricted by slower internal gravity wave speeds $c_{\rm i} \approx (g\Delta\rho D/\rho_0)^{1/2}$. For details and the governing equations see the POM User's Guide by Mellor (2002a). The only difference that will be used later to specify fresh water is to include a vertical velocity $w_{\rm River} \leqslant 0$ to the RHS of the external-mode continuity equation (and appropriate changes to the salinity and temperature equations; Oey, 1996; O2005). For WAD processes, code changes to the external-mode equations for η and the depth-averaged velocity $(\overline{U}, \overline{V})$ are essential.

Suppose we begin the model simulation with leveled free surface (at the msl), so that $\eta = -H_{\rm hi}$ and $H \leqslant H_{\rm hi}$ (i.e. $D \leqslant 0$) defines (x,y) where the cell is dry but where WAD processes can occur. We set the mask FSM $= 0$ at ∂R (and landward of ∂R) but FSM $= 1$ at all other cells including potential WAD regions, dry or wet. We then define another mask:

$$\begin{aligned} \text{WETMASK} &= 0 \quad \text{for } D \leqslant H_{\rm dry}, \\ &= 1 \quad \text{otherwise.} \end{aligned} \tag{2.3}$$

The $H_{\rm dry} = 0$ for the purpose of discussion, but is O(cm) in the code as will become clear shortly. Unlike FSM, WETMASK distinguishes between dry (=0) and wet (=1) cells; note WETMASK = FSM at ∂R. The use of WETMASK greatly facilitates WAD implementations. At each $\Delta t_{\rm e}$, after $(\eta, \overline{U}, \overline{V})$ are updated, we update D and apply (2.3). The condition that there can be no fluxes across a dry cell-face is then imposed. On a *C*-grid (Fig. 2) checks are applied separately at the $\overline{U}$ and $\overline{V}$ cell-faces. Thus,

$$\overline{U}_{i,j} = 0 \quad \text{if } (D_{i,j} + D_{i-1,j})/2 \leqslant H_{\rm dry} \tag{2.4a}$$

$$\overline{V}_{i,j} = 0 \quad \text{if } (D_{i,j} + D_{i,j-1})/2 \leqslant H_{\rm dry} \tag{2.4b}$$

Note that we do not specify the value of η at dry cells (i.e. the first of (2.3)). Because of (2.4), η at a dry cell remains at its value from the previous time step.

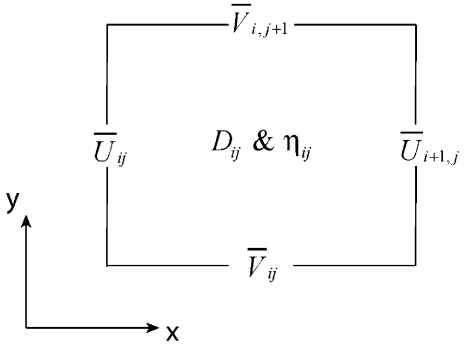

Fig. 2. The C-grid. The D_{ij} or η_{ij} point is also where $\mathrm{WETMASK}_{ij}$ is defined.

The code solves the full set of governing equations over wet as well as dry cells (and, for that matter, land cells also). Since POM's time-stepping involves D^{-1}, it is necessary that $H_{\mathrm{dry}} \neq 0$. However, this is a coding artifice, removable at the expense of recoding using $D(\overline{U}, \overline{V})$ rather than $(\overline{U}, \overline{V})$ as the primary variables. On the other hand, it is useful to think of the dry cells as having a thin film of fluid of thickness $= H_{\mathrm{dry}}$. At each time step, flows across previously dry cell faces satisfy the force balance (momentum) equations, which dictate if the dry cells become wet. Dry cells are thus temporarily dormant, to be activated dependent on volume and momentum (heat and salt also for general stratified flows) conservations in that cell as well as in the neighboring cells. Fig. 3 (cases A and C) illustrates these ideas assuming for simplicity that pressure gradient balances friction. In actual simulations, the WAD checks are made using the full primitive equations. This enables, for instance, face "i" to open with $U_i < 0$ even in case B (Fig. 3) due to, say, sufficiently strong westward wind or U_{i+1}, so that wind and momentum advection (or both) can dominate the adverse elevation gradient.

Conditions (2.3) and (2.4) are all that were required for the idealized WAD cases considered in O2005. In more general cases (e.g. realistic bathymetry with winds), the following additional condition enhances the robustness of the model. When the $\overline{U}$ and $\overline{V}$ cell-faces are not dry (i.e. (2.4) is not satisfied), yet at least an adjacent cell is dry, we set the corresponding velocity at that face $= 0$ if there is an outflux from the dry cell. This last condition arises because the D and $\overline{U}(\overline{V})$ are not defined at the same position, and a physically unrealistic outflux from a dry cell must be shut off (Fig. 3, case B); thus,

$$\overline{U}_{i,j} = 0 \quad \text{if } \mathrm{WETMASK}_{i-1,j} = 0 \text{ and } \overline{U}_{i,j} > 0, \text{ or, } \mathrm{WETMASK}_{i,j} = 0 \text{ and } \overline{U}_{i,j} < 0. \tag{2.5a}$$

$$\overline{V}_{i,j} = 0 \quad \text{if } \mathrm{WETMASK}_{i,j-1} = 0 \text{ and } \overline{V}_{i,j} > 0, \text{ or, } \mathrm{WETMASK}_{i,j} = 0 \text{ and } \overline{V}_{i,j} < 0. \tag{2.5b}$$

The anomalous outflux is purely numerical (due to truncation and round-off errors), and does not exist in the continuous equations as pressure gradient force is nil across a dry 'face' (where $D = 0$).

2.3. Internal-mode conditions

The (external-mode) conditions (2.3)–(2.5) are necessary in the WAD scheme used here. They are insufficient for the general three-dimensional baroclinic flows. Two additional conditions and two auxiliary implementations are required. The first condition is that in dry cells the temperature and salinity of the thin film relax to their climatological values:

$$\frac{\partial T}{\partial t} = -\alpha_{\mathrm{relax}}(T - T_{\mathrm{clim}}) \quad \text{if } \mathrm{WETMASK} = 0, \tag{2.6}$$

and a similar equation for S, where $\alpha_{\mathrm{relax}} = 2\ \mathrm{day}^{-1}$ is used. Other schemes that book-keep dry-cell T/S (e.g. set to values when the cell was last wet; provided that the time interval between two separated wet events at the particular cell is reasonably short (say 1 day), for otherwise the last wet values may have little to do with the

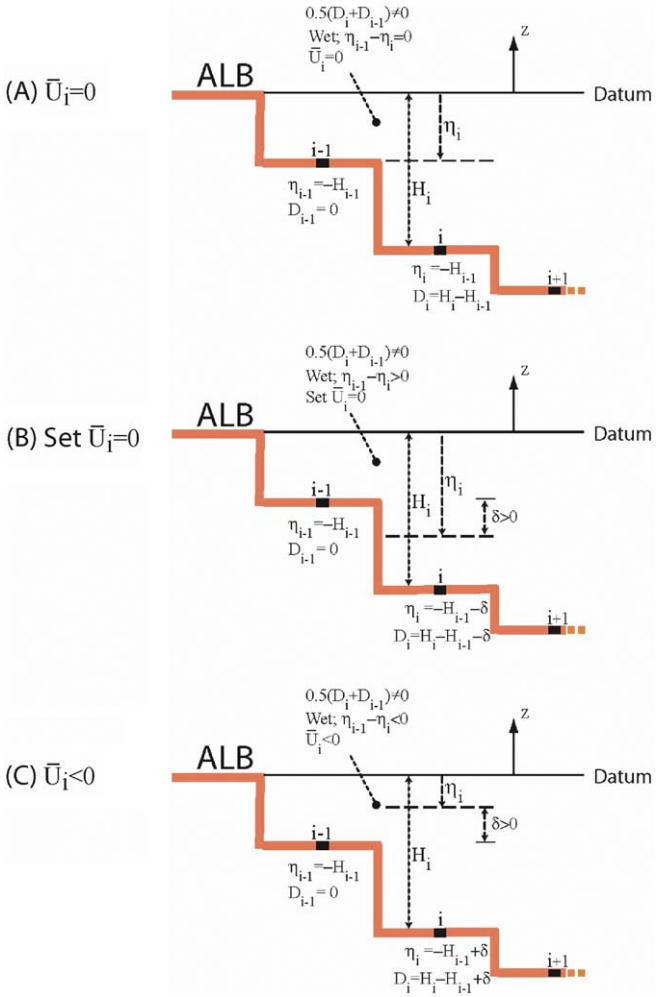

Fig. 3. A schematic of how Oey's (2005) wetting and drying scheme determines flow velocity $\overline{U}_i$ at the cell-face between cells "$i-1$" (dry) and "i" (wet) assuming that pressure gradient is balanced by friction: $\overline{U}_i \propto (\eta_{i-1}-\eta_i)$. (A) is when the free surface at "i," η_i, is leveled with the bottom of cell "$i-1$" inducing no pressure gradient, hence $\overline{U}_i=0$; (B) is when η_i drops below the bottom of cell "$i-1$" inducing a false pressure force from cell "$i-1$" to "i" and an anomalous $\overline{U}_i$ that must be set zero (condition (2.5) in text); the anomalous error tends to zero for sufficiently smooth solution (i.e. with refined grid); (C) is when η_i rises above the bottom of cell "$i-1$" inducing a pressure force from cell "i" to "$i-1$", hence $\overline{U}_i<0$ (see text).

next wet-field conditions) would also work. Eq. (2.6) is used for its physical implications that, after being isolated from other wet cells, hence exposed to the atmosphere, the thin film of fluid in a dry cell adjusts to its surroundings, for which the T_{clim} should $\approx T_{\text{air}}$, the air temperature. From a coding perspective, dry-cell T/S are used at future times should the cell become wet.

The second condition requires that there can be no vertical (baroclinic) velocity structures across a dry cell's faces, e.g.:

$$\begin{aligned} U_{ijk} &= \overline{U}_{i,j} \quad \text{if } \text{WETMASK}_{ij} * \text{WETMASK}_{i-1,j} = 0, \quad \text{and} \\ V_{ijk} &= \overline{V}_{i,j} \quad \text{if } \text{WETMASK}_{ij} * \text{WETMASK}_{i,j-1} = 0, \quad \text{for all } (i, j \text{ and } k), \end{aligned} \tag{2.7}$$

where k is the vertical grid index. This condition is stricter than the corresponding one for the depth-averaged velocities, condition (2.4), but is necessary in order to prevent spurious shears from developing across dry-cell faces at (transition) times when the dry cell becomes wet. Physically, the assumption of a purely barotropic flow (in very shallow water) under that situation is an excellent one. With condition (2.7), we also eliminate

velocity "overshoots" that sometimes can occur at a dry-cell face during transition to becoming wet (e.g. Stelling and Duinmeijer, 2003).

Finally, there are two auxiliary implementations: one deals with how the WETMASK is defined in a time-split integration, and the other with bottom shear-stress specification when cells are drying and fluid becomes very thin. Details are given in Appendix A. Conditions (2.3)–(2.7) and the auxiliaries (in Appendix A) complete the WAD implementations in POM. The same algorithm should apply to other models that use split-time step, *C*-grid and *sigma*-coordinate.

3. Tests

For all tests, $H_{\rm dry} = 5$ cm and $z_0 = 1$ cm. Sensitivity of solutions to $H_{\rm dry}$ is described in O2005. A finite $H_{\rm dry}$ (O(cm)) smoothes the transition between dry and wet cells, in contrast to other WAD schemes (see e.g. Falconer and Owens, 1987). The reason for the difference is not clear, but maybe because our WAD scheme makes less distinction between dry and wet cells by utilizing the full primitive-equation set for WAD checking. In the following tests, the goal is to subject the model to a series of forcing of relevance to WAD processes: wind, sea-level (tides and tsunami) and stratification, and to check conservation properties.

3.1. Test 1

Water flows down a slope into an initially dry basin. The water is homogeneous and the depth-averaged equations only of the model are used. The model domain (Fig. 4A) is rectangular 150 km × 200 km with walls on all four sides on an *f*-plane ($f = 7.5 \times 10^{-5}$ s^{-1}). There is a bay in the north: 200 km $\geqslant y \geqslant$ 160 km with sloping shelf in its western portion (Fig. 4C), a sill at $y = 160$ km, and a tanh-shape slope for 160 km $\geqslant y \geqslant$ 80 km over which the topography drops by 137.5 m, and thereafter remains constant to the southern wall at $y = 0$ (Fig. 4B). The horizontal grid sizes $\Delta x = \Delta y = 1$ km. The domain is initially filled with water in the bay, at rest and water depth $D = 37.5$ m just below the sill, and is dry everywhere else. A constant downward velocity $w_{\rm River}$ (<0) is specified over each grid cell of the bay such that the total volume flux $Q = 3 \times 10^4$ m^3 s^{-1}. A sinusoidal zonal (x) wind stress with amplitude = 2 dyn cm^{-2} (roughly 10 m/s wind) and period = 5 days is specified uniformly over the bay. Under these forcing, the bay's water spills down the slope and floods the basin below. The integration was carried out for 30 days. Bottom friction = 0 and a small horizontal viscosity = 10 m^2 s^{-1} is used. Auxiliary runs with wind = 0, $f = 0$ and/or $Q = 0$ were also conducted (below). The trivial case $Q = 0$ with no wind was run to confirm $(U, V) = 0$ and southern basin remaining dry for all time.

The left panel of Fig. 5 shows water depth and velocity vectors at $t = 1$ day, and the right panel shows the corresponding x-averaged U, V and D as functions of y. The flow accelerates down-slope, and maximum speeds exceed 6 m s^{-1} over the slope where the layer thins to less than 0.1 m, i.e. super-critical. The flow then becomes sub-critical through a series of hydraulic jumps that give rise to sporadic WAD on the slope (cf. Baines, 1995). Smolarkiewicz (1984) positive-definite scheme used for total water depth also gives sporadic WAD; the physics is interesting though it is not the goal of this paper. The flow spreads and the layer thickens (≈0.2 m) over the flat portion of the basin. For these strong flows, the Coriolis term fv is not negligible even at early times and the flow veers west ($U \approx -0.6$ m s^{-1}; the $U \approx 0$ m s^{-1} for the $f = 0$ case, not shown). The integration remains stable despite these extreme conditions. The (initially dry) basin gradually fills to about 8 m over 30 days (not shown).

Without loss of generality, volume and energy conservations are shown here for the simpler case of wind = 0. Appendix B gives the formulae. A useful domain $\mathscr{A}$ (Eq. (B.1)) is the initially dry (southern) basin bounded by the sill, since this includes a large WAD region and $q = 0$. The line integrals along the sill are non-zero given by volume and energy fluxes from the northern bay. (The conservation properties are not changed when $\mathscr{A}$ is taken as the whole basin and q included). It turns out that (without wind) fluxes over the sill are nearly constant so that both volume and energy are linear with time as shown in Fig. 6. Note that because of the way η is defined (i.e. below the datum, Fig. 1), η^2 is largest at $t = 0$, and downward-sloping energy curve (Fig. 6) actually means increasing (potential) energy as the basin fills up. The figure shows good agreements between the computed values (solid lines) and those estimated based on influxes (of energy and volume) across the sill from the northern bay (dotted lines). The difference in the equivalent height $\left(\int\int_A D\,{\rm d}x\,{\rm d}y / \int\int_A {\rm d}x\,{\rm d}y\right) \approx$

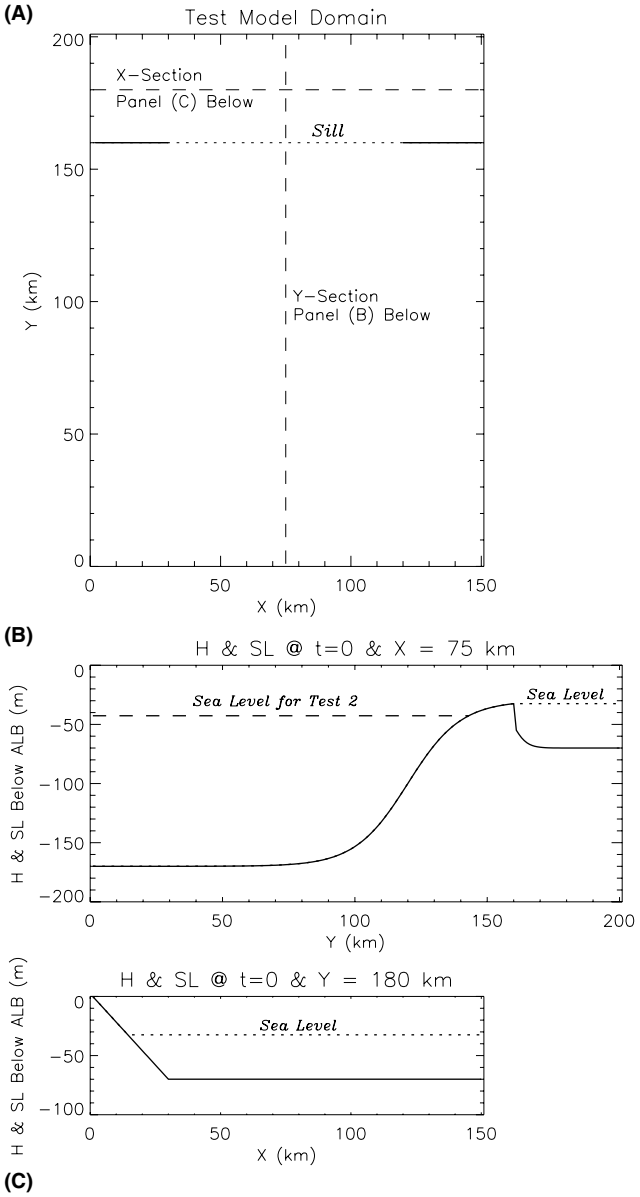

Fig. 4. Model domain, topography (H) and sea levels (SL) used in tests 1–3. Initial SL in the northern bay is shown as dotted line in (B) and (C). For test 1, the southern basin is initially dry while for tests 2 and 3 the SL is shown as dashed line. See text for details.

2.5 ± 0.9 cm is within the uncertainty of $H_{\mathrm{dry}} = 5$ cm, and in energy it is less than $(0.1 \pm 2)\%$ of the energy increase over 30 days. Energy conservation is a more stringent test (Stelling and Duinmeijer, 2003).

3.2. Test 2

This has the same configuration as Test 1 except that the bay is initially filled with less-saline water $S = 20$ psu, the southern basin with $S = 36$ psu filled to 10 m below the sill (see panel B of Fig. 4) and the full three-dimensional equations (but $T = 10$ °C, a constant) are used with 21 equally spaced *sigma* levels in the vertical. Bottom friction is non-zero (with $z_0 = 0.01$ m; Appendix A). I show here the case for wind $= 0$ and fresh water ($S = 0$) discharge $Q = 3 \times 10^4$ m^3 s^{-1} applied to the northern bay (as before); the non-zero

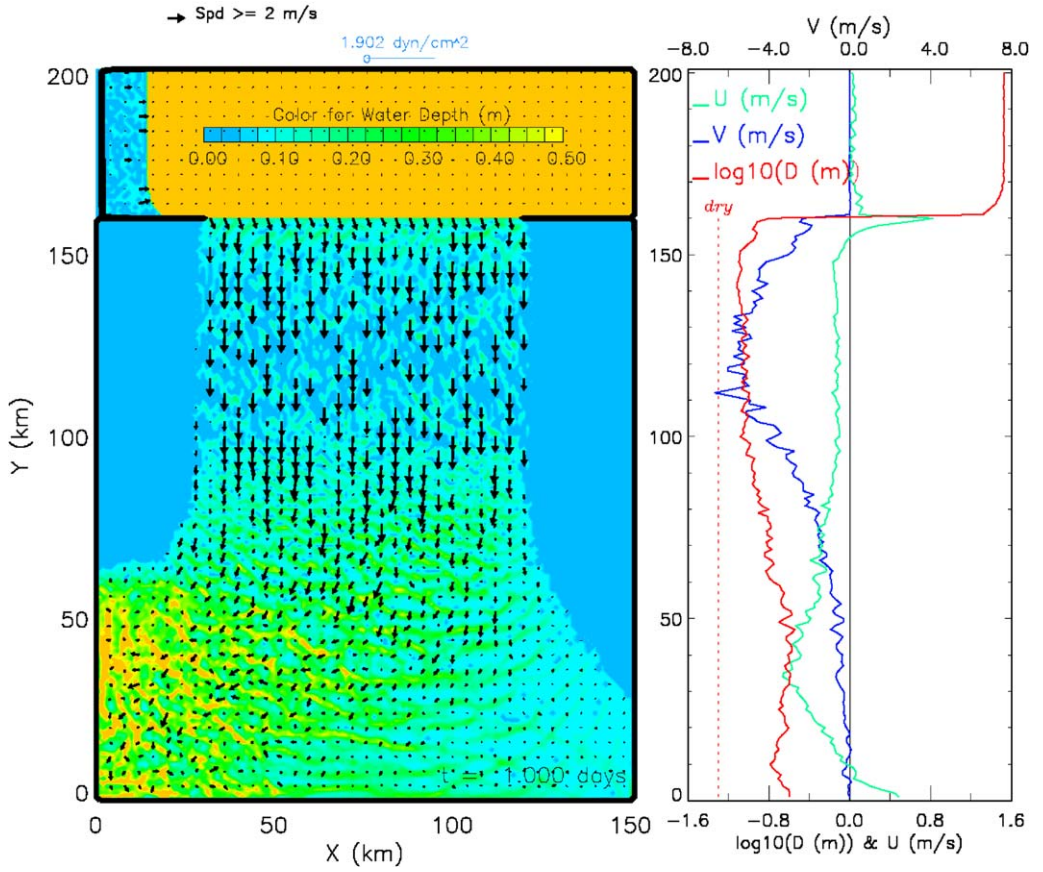

Fig. 5. Test 1: Flow slopes down into an initially dry basin at $t = 1$ day after spillage over the sill at $y = 160$ km. Left panel: water depth D in color (blue is dry and yellow for $D > 0.5$ m) and velocity vectors plotted at every four grid points. Wind vector is shown at top of panel. Right panel: x-averaged U, V, and D expressed as $\log_{10}(D)$ (to show its full range $0 \leqslant D \leqslant 37.5$ m).

wind case has also been run with no difficulties. Note that Q is discontinuous across the sill, and there will also be a corresponding discontinuity in the solution for S. The problem of fresh-water debouching into a body of saline water, without WAD, is well-studied (e.g. Chao and Boicourt, 1986; Oey and Mellor, 1993). The experiment is idealized but is a good test case for the WAD scheme, as it contains elements such as three-dimensionality, strong stratification and topography.

Fig. 7 shows S and (U, V) at the first *sigma-level* (surface) at day 1, 10, 20 and 30. There is down-shelf flow in the western portion of the northern bay due to discharge of fresh water, as well as down-slope flow over the sill of less-saline water spreading over the saline body of water in the southern basin. Because of the (spatial) discontinuity in Q water in the bay is fresher than water over the slope; both continue to freshen with time. At early times (day 1), the S-profile develops 'wiggles' ($\approx\pm 1$ psu) as the flow races down-slope and adjusts to the strong jump ($\approx$20–36 psu). These numerical oscillations disappear with time. At day 10, a wide anti-cyclonic plume develops under the influence of Coriolis at the foot of the slope, and coastal current develops around the basin; the propagation speed $\approx 0.4\ \mathrm{m\ s^{-1}}$. The plume depth ≈ 5 m, which yields a first-mode baroclinic phase speed $\approx 0.5\ \mathrm{m\ s^{-1}}$ (cf. Chao and Boicourt, 1986). The coastal flow coalesces with the plume at day 20 and the resulting jet (at $x \approx y \approx 120$ km) entrains fresh water into the saline pool to form an interior anticyclonic eddy at day 30. Note that anticyclonic flow develops in the northern bay forced by the source term Q.

The model without WAD conserves salt (or any tracer) so we check that the code with WAD retains this property. Fig. 8 (upper panel) shows that Eq. (B.4) is satisfied and also that $\overline{S}(t)$ is decreasing with time (Eq. (B.5)). For completeness, the lower panel of Fig. 8 shows that volume is conserved; differences in the equivalent height from volume computed from Q are ≈ 1 cm.

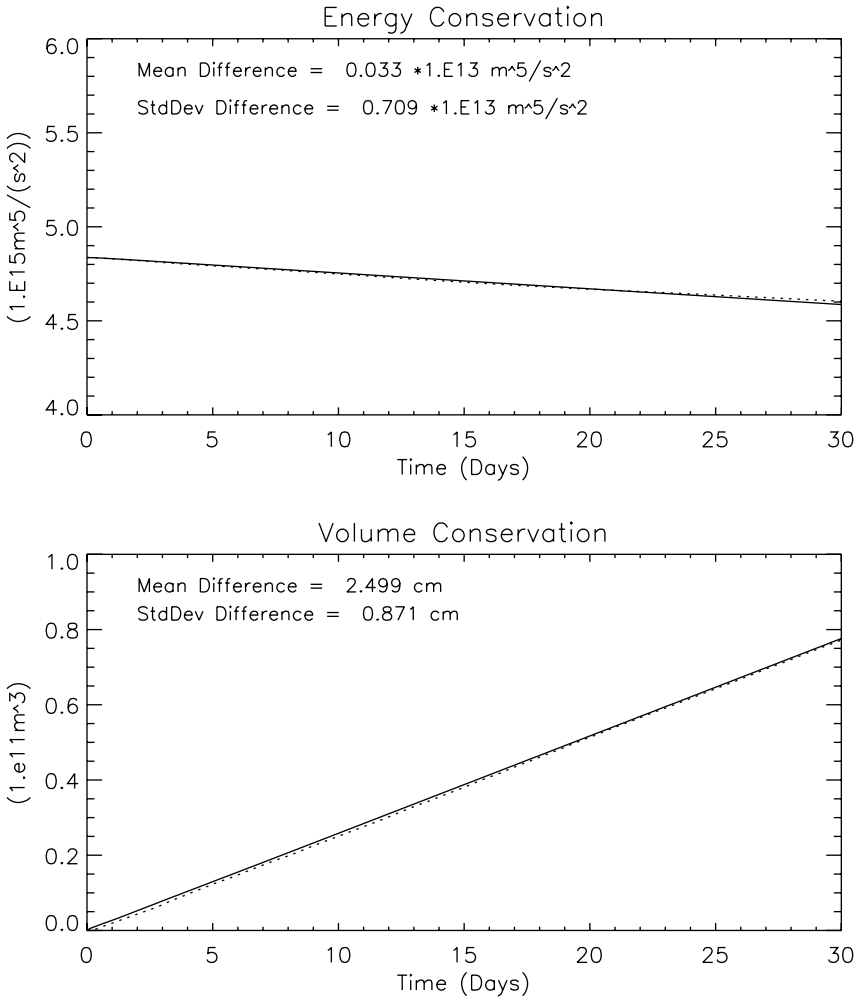

Fig. 6. Test 1 without wind: Energy and volume conservation plots for the initially dry (southern) basin. Solid curves are values calculated directly from the model results. Dotted curves are estimates based on influxes (of energy and volume) across the sill from the northern bay. The mean and standard deviation of the difference (equivalent height for the volume conservation) are printed in each panel. See text for details.

3.3. Test 3

This has the same configuration as Test 2 except that the southern boundary is now open and tide (period = 12 h) is specified (see Oey and Chen, 1992 for the open-boundary specifications). Two experiments were carried out. One (Test 3a) has a moderately strong tidal current (amplitude ≈1 m/s) that at high tide the sea rises 5 m above the initial level which is at 10 m below the sill; thus saline water does not intrude into the bay. Another experiment (Test 3b) doubles the tide (amplitude ≈2 m/s) and at high tide the sea rises up to the sill. The objective is to demonstrate the robustness of the WAD scheme under these rather extreme mixing and stratification conditions. Each experiment was carried out for 20 tidal cycles (10 days).

Fig. 9 shows the surface S and (U, V) at the last cycle and may be compared with Fig. 7. Advection and mixing by tides have made the plume and coastal current boundary less sharp. WAD processes occur over the slope, and can be seen most clearly in the northwestern and northeastern corner regions of the main basin. An example is given in Fig. 10, which plots vertical section contours of (U, V) and S at $x = 15$ km for 130 km $\leqslant y \leqslant$ 160 km. The figure shows wetting and drying of the slope as the tide floods then ebbs. Note the dry portion of the slope indicated by the dark topographic line and also the thin-layer region which is

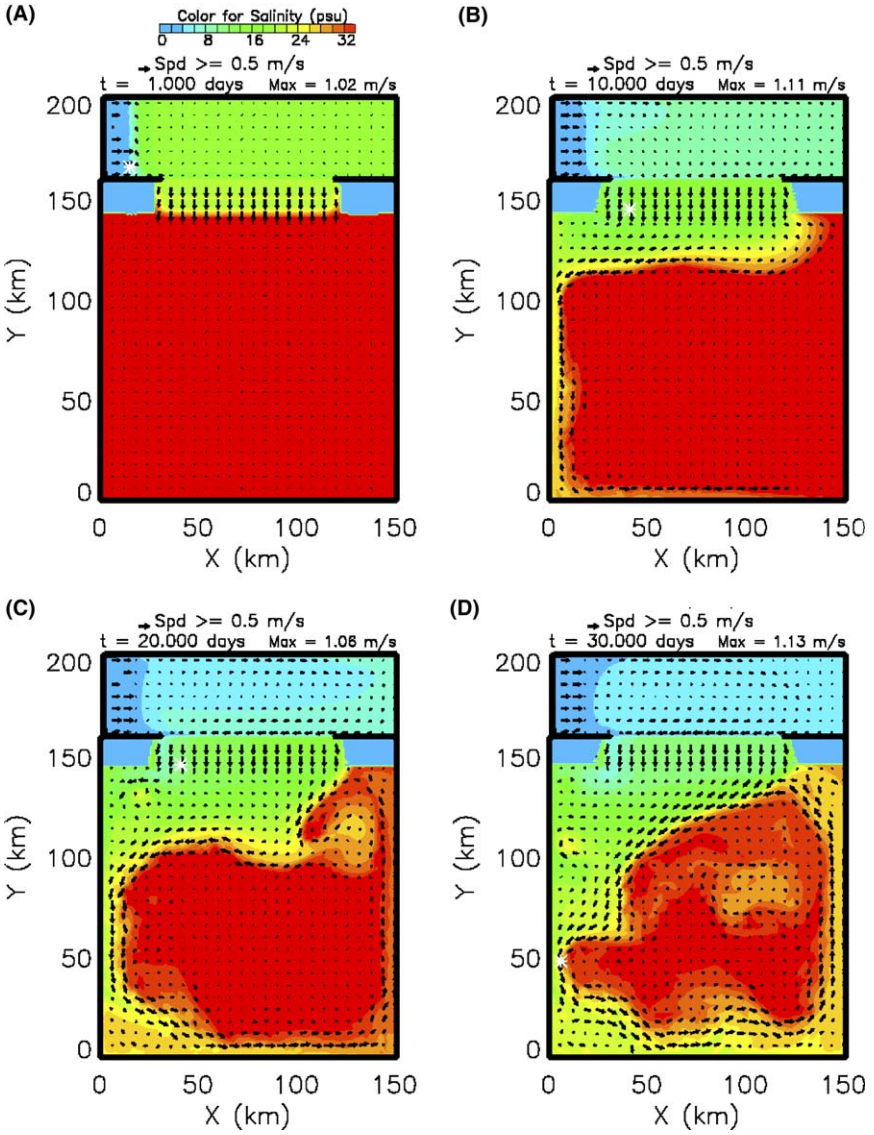

Fig. 7. Test 2: Spillage of less-saline water ($S \leqslant 20$ psu) from the northern bay over the sill and slope to the southern basin that initially contains salty water ($S = 36$ psu). Plotted are surface salinity and velocity vectors at surface (*sigma-level* 1) at time (A) 1 day, (B) 10 days, (C) 20 days and (D) 30 days after the spillage at $t = 0$. White asterisk shows location of maximum speed, and the value is printed on top of each panel.

nonetheless still wet. This water-retention property of the WAD physics is caused by bottom friction which creates tidal asymmetry and also net down-slope currents (O2005). Physically, for thin layer over slope, $D \ll 1$, $|\partial D/\partial y| \ll |\partial H/\partial y|$ and the term $g(\partial H/\partial y)$, which is force per unit mass due to gravity in the down-slope direction, drives the flow. While tides in Test 3a remain over the lower slope, we find that Test 3b's strong tides penetrate into the northern bay, providing a means by which fresh water is flushed out down the slope (not shown).

3.4. Test 4: A tsunami model

Tsunamis are surface waves caused by earthquakes or other catastrophic events (e.g. landslides) in the ocean (Ward, 2001). They are predominantly long waves, $kH \ll 1$ where k is the x-wavenember (in

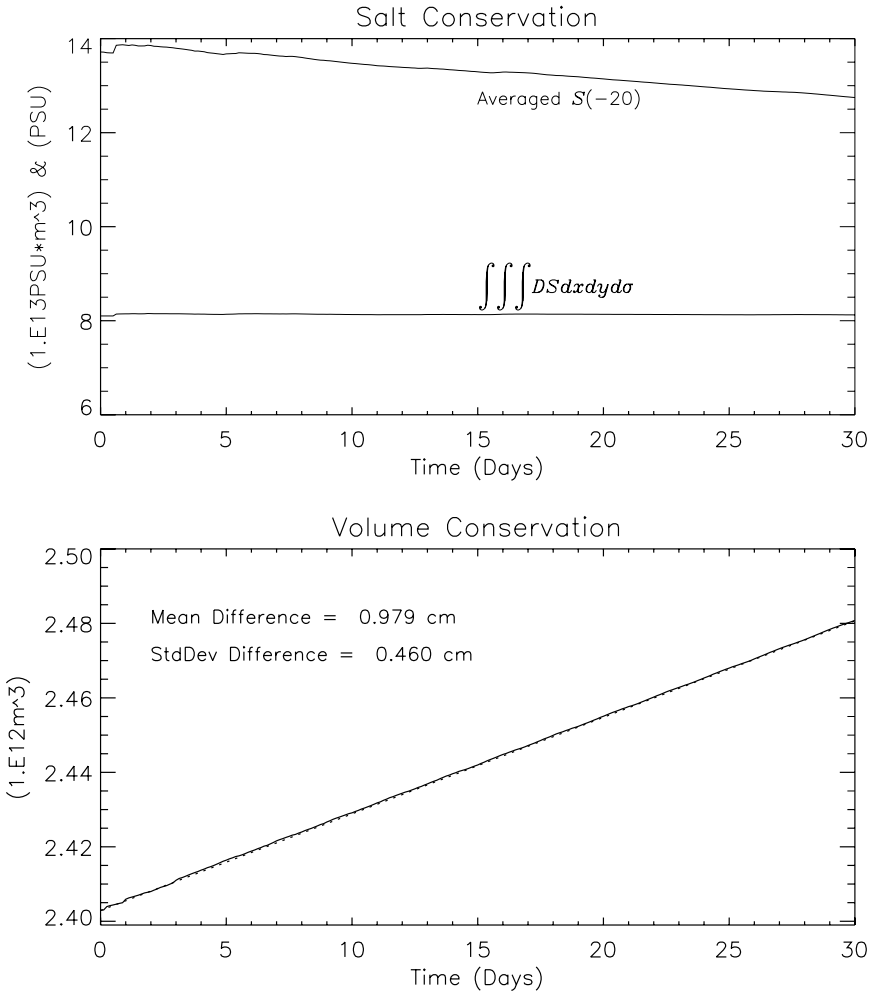

Fig. 8. Test 2: Salt and volume conservations.

one-dimensional case), that travel vast distances at the maximum group velocity $c_s = (gH)^{1/2}$ and are weakly dispersive. (It is convenient in this subsection to revert to the conventional definitions of H and η referenced with respect to the mean sea level.) Dispersion leads to the linear KdV equation (the leading two terms of dispersion relation contain k and k^3) and a solution (e.g. for an initial pulse) involving the Airy function. This decays exponentially ahead of the front $x - c_s t > 0$, and oscillatory behind (Witham, 1974; see also LeBlond and Mysak, 1978 and Gill, 1982). Being hydrostatic, our model cannot describe tsunami dispersion, but should give a good approximation once the front propagates onto the shelf. Shoaling and embayment lead to further energy concentration near the tsunami front that can cause severe destruction as it hits land with large amplitudes and strong current speeds. "Trailing wave ripples" result in repeated hits and the subsequent equally intense run-down speeds cause further human sufferings. WAD is an integral part of tsunami modeling.

The objective is to show that the WAD scheme developed herein can handle intense wave run-up (run-down) processes; no attempt is made to address the accuracy or physical reality. Tsunami models employing shallow-water equations generally specify initial distribution of sea-surface that relates, in the case of an earthquake for example, to the initial disturbance at the bottom (Titov and Synolakis, 1997). Tests with both idealized and realistic bathymetry were conducted. The idealized case of (channel) propagation of an initial step function from the open ocean over a sloping beach and onto the land is presented here.

The ocean is assumed barotropic. Initially, an elevated sea-surface $\eta_0 = 5$ m high is specified for $0 \leqslant x \leqslant l_0 = 3$ km near the closed end of the channel at $x = 0$ where its width $B(x = 0)$ is 500 km and the water

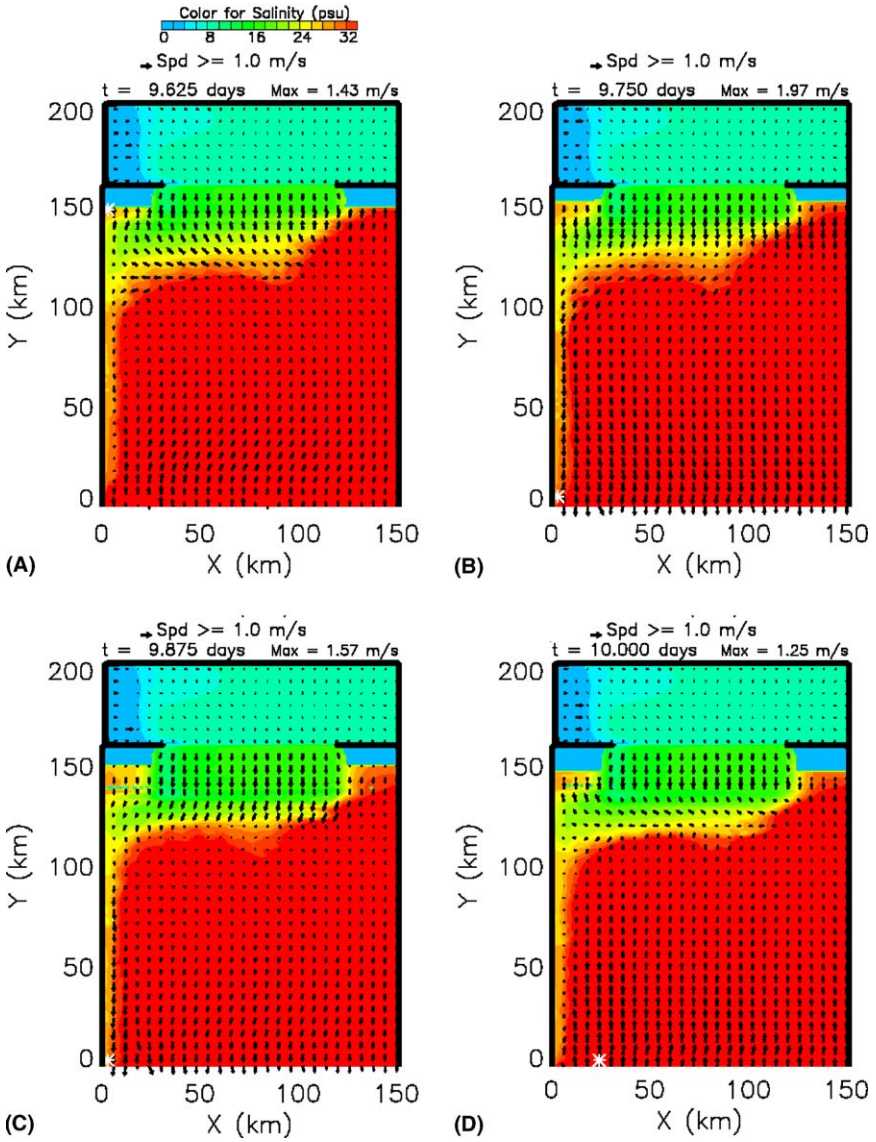

Fig. 9. Test 3a: Tidal mixing of spillage of less-saline water ($S \leqslant 20$ psu) from the northern bay over the sill and slope to the southern basin that initially contains salty water ($S = 36$ psu). Plotted are surface salinity and velocity vectors at surface (*sigma-level* 1) at every 3 h of the last tidal cycle, 9.5–10 days. White asterisk shows location of maximum speed, and the value is printed on top of each panel.

depth is 100 m. The channel's width narrows to 50 km at $x = 32$ km and remains constant thereafter. For uniform H and B (in the infinite half plane $x > 0$) the initial step propagates to the right ($x > 0$) and spreads to double its length (to $2l_0 = 6$ km) and half its height (to $\eta_0/2 = 2.5$ m) in $t = l_0/(gH)^{1/2}$ (Gill, 1982). (This linear solution was numerically verified to ensure that oscillatory solution below is not due to numerical dispersion.) Shoaling ($\partial H/\partial x < 0$) leads to concentration of energy near the propagating front (the right face of the step) with small-amplitude trailing oscillations, and the length also shorten (back to l_0) and amplitude increases. Non-linearity accentuates wave steepening and oscillations. Narrowing of the channel's width ($\partial B/\partial x < 0$) increases the wave amplitude. To estimate the wave height just before land fall, we equate the initial energy to the energy at time t assuming that the latter is concentrated within $x_1(t) \leqslant x \leqslant x_2(t)$:

$$g\eta_0^2 \int_0^{l_0} B\,\mathrm{d}x = \int_{x_1}^{x_2} B(g\eta^2 + Du^2)\,\mathrm{d}x. \tag{3.1}$$

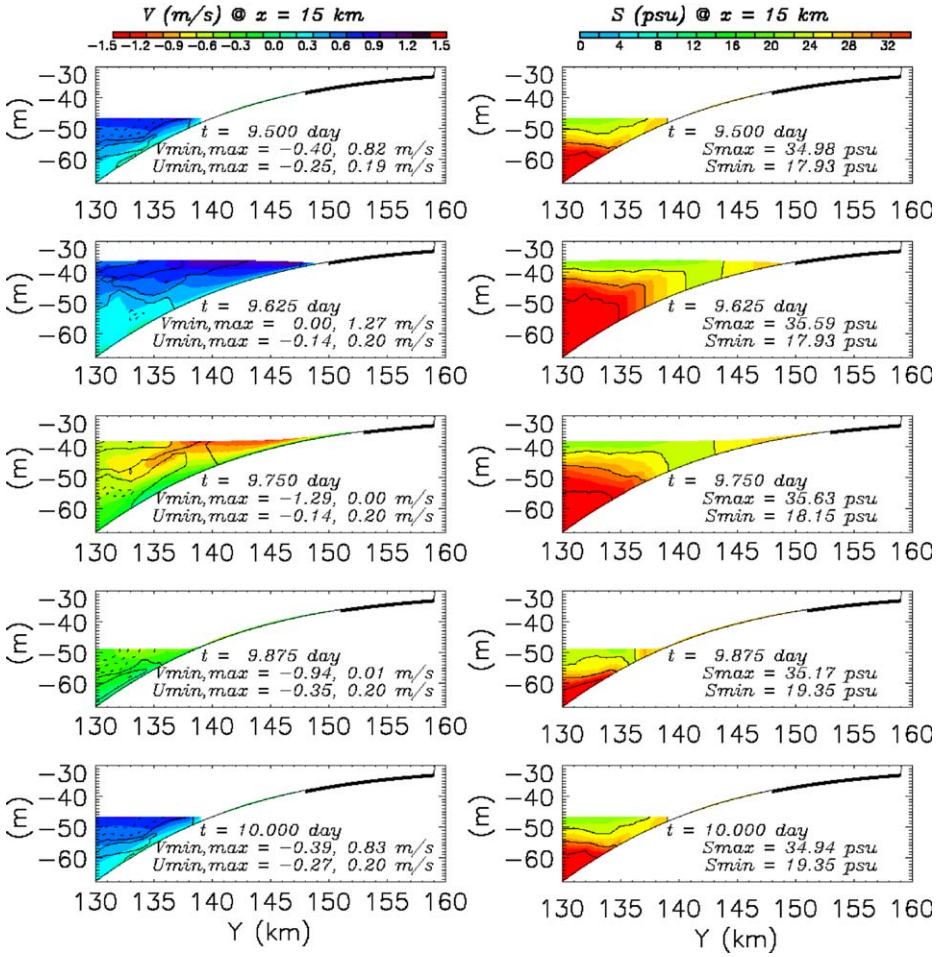

Fig. 10. Test 3a: *YZ*-vertical section contours of U (contour interval = 0.1 m/s, dotted is negative) superimposed on color images of V (left panels) and S (right panels color, contours indicate 34, 28, 22, 16 and 10 psu) at $x = 15$ km in the northwestern corner region where WAD prevails, at the indicated times over the last tidal cycle of the model integration. The dark line over the upper slope indicates dry cells.

A good approximation is that $x_2 - x_1 \approx l_0$ and both are sufficiently narrow that B is locally a constant. Then defining an average over $[x_1, x_2]$ (denoted by overbar) of the integrand on the RHS of (3.1) one obtains:

$$\overline{\eta^2} + \frac{\overline{Du^2}}{g} \approx 2\overline{\eta^2} \approx \eta_0^2 \frac{B_0}{B(\bar{x})}, \tag{3.2}$$

where $B_0 = B(x = 0)$ and I have also used the linear result that for step-propagation the energy is equally distributed between kinetic and potential. For the model, $B_0/B \approx 10$ near the shore, so that before land-fall $\bar{\eta} \approx 2\eta_0 \approx 10$ m $\approx \overline{D}$, and the current speed $\bar{u} \approx 14$ m/s.

Fig. 11A shows the model domain, and subsequent panels show fields at the indicated times in a magnified region (enclosed in dashed rectangle in Fig. 11A) that includes the (initial) shoreline. Grid size $\Delta x = 0.25$ km and both the original center-space differencing scheme of POM and Smolarkiewicz (1984) positive-definite scheme were tested. Only small differences were found between the two results. Smolarkiewics' scheme is shown here. At $t = 18.75$ min, the peak wave amplitude $\eta_{\text{peak}} = 12.6$ m at about 10 km from the shore (Fig. 11B). This amplifies to 14.5 m before diminishing to 11.4 m at land-fall, with speeds ≈10–16 m/s (Fig. 11C and D). These values are in fair agreements with those estimated above. The up-land propagation occurs with very strong currents ≈17–20 m/s (Fig. 11E and F). The receding phase consists of smaller-amplitude waves ≈2–3 m but the currents are again very strong ≈−15 m/s (Fig. 11G–I). As the receding water

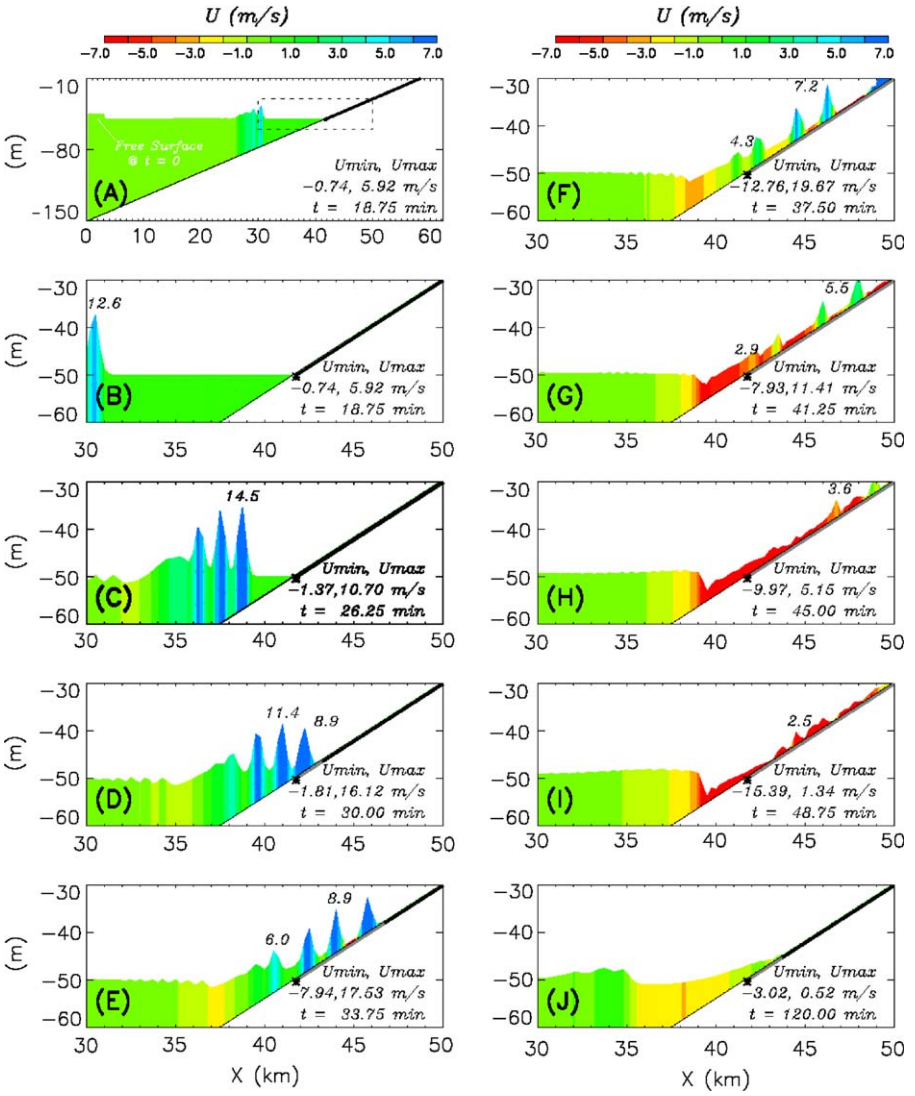

Fig. 11. Simulation of tsunami propagating onto a sloping beach and over the land. Colors are *XZ*-section contours of *U* which also show wave-height at the indicated times in minutes. Panel A shows the full-domain field at $t = 18.75$ min and the initial wave-height. Fields within the dotted rectangle are magnified in panels B–J at various times. Numbers indicate wave-heights in meters, referenced with respect to the mean sea-level over the ocean and to the local land elevation on land. The maximum and minimum *U* are printed in each panel. Thick black line indicates dry land while gray land that has become wet. Position of initial shoreline is marked as '∗'.

plunges back to the ocean, a bore-like feature is seen propagating out to the open sea (Fig. 11I and J). At $t = 120$ min, most of the water has receded and wet cells become dry again (Fig. 11J).

3.5. Test 5: A model of the Cook Inlet, Alaska

We have applied the WAD scheme to simulate two and three-dimensional processes using realistic bathymetry of the Cook Inlet, Alaska (Fig. 12 shows a locator map). An example of a three-dimensional simulation with tide, fresh-water and wind forcing is now given. Accurate bathymetry is important in modeling WAD processes in a realistic estuary. A high-resolution (0.5 km × 0.5 km) topographic dataset is used.

Water levels and currents in the Cook Inlet are strongly influenced by tides from the Gulf of Alaska through the Stevenson–Kennedy entrance, the M_2 tide (period $P \approx 12.42$ h) in particular. Taking a rough

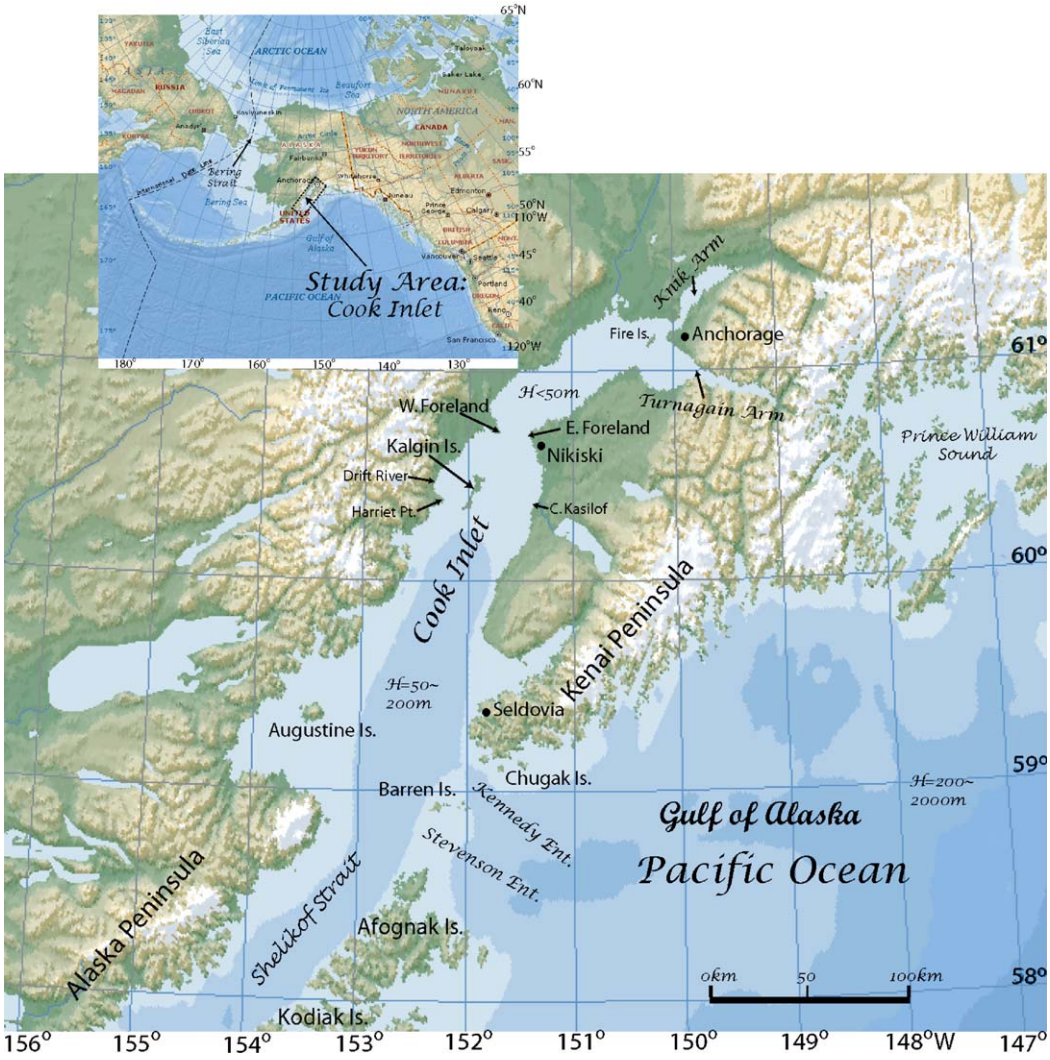

Fig. 12. The Cook Inlet locator map with crude (cartoon-like) outlines of bottom depths.

value of 50 m for the Inlet's averaged water depth H_{ave}, the 'tidal resonant' length $\approx (gH_{ave})^{1/2}P/4 \approx 240$ km (Gill, 1982), which is close to the Inlet's distance from Stevenson–Kennedy entrance to the upper inlet. Thus tides tend to amplify in the upper inlet. Observed tidal range at Anchorage is $\approx \pm 5$ m, while near the Stevenson–Kennedy entrance the range is $\approx \pm 1$ m. The large tidal range and generally shallow depths in the upper inlet gives rise to extensive mudflats especially in the Knik and Turnagain Arms. In addition to tides and WAD, currents induced by buoyancy (from rivers and snowmelt) and winds also constitute important components of the circulation and mixing in the Cook Inlet. The combined high discharge during spring/summer snow-melt amounts to over 5×10^3 m^3 s^{-1}. Freshening and tidal and wind mixing result in a near-surface salinity $S \approx 30$–32 psu at the Stevenson–Kennedy entrance, approximately the values found over the adjacent shelf/slope in the Gulf of Alaska (Xiong and Royer, 1984). The Cook Inlet/Gulf of Alaska climate is extreme. Winter storms due to the Aleutian Low propagate eastward. These storms and continental drainage winds bring high wind speeds (over 20 m s^{-1}) and low temperatures. The mean winter wind is generally westward. In summer, the Aleutian low is replaced by a weak anticyclonic system, resulting in generally eastward (and much weaker) wind (Royer, 1975). There is also considerable high-frequency variability.

The topographic dataset was interpolated onto a 401×151 grid (approximately along and across-inlet) that covers the entire Cook Inlet from Stevenson–Kennedy Entrance and Shelikof Strait to Knik and Turnagain

Arms in the upper inlet. Grid sizes vary from 1 to 2 km in the lower inlet to less than 0.5 km in the upper inlet. The test uses the complete three-dimensional WAD code and simulates tide, wind and buoyancy-driven (i.e. from rivers and snowmelt) circulation in the Cook Inlet. A hypothetical tide with 1 m amplitude and 12 h period is specified at the open-ocean boundaries at Stevenson–Kennedy entrance and Shelikof Strait, where climatological temperature and salinity are also specified during inflow. Hourly winds corresponding to year 2000 from NOS and NOAA stations in the Inlet are interpolated onto the model grid, and maximum river discharges are used (total $\approx 5 \times 10^3$ m^3 s^{-1}) distributed primarily over the upper inlet (many over otherwise dry cells). To demonstrate robustness, the model was integrated for 1 year with the constant high-discharge forcing, during which the model Cook Inlet establishes its own salinity (and temperature) and circulation structures. Fig. 13 shows plots of near-surface salinity and velocity vectors during flood (panels A and B)

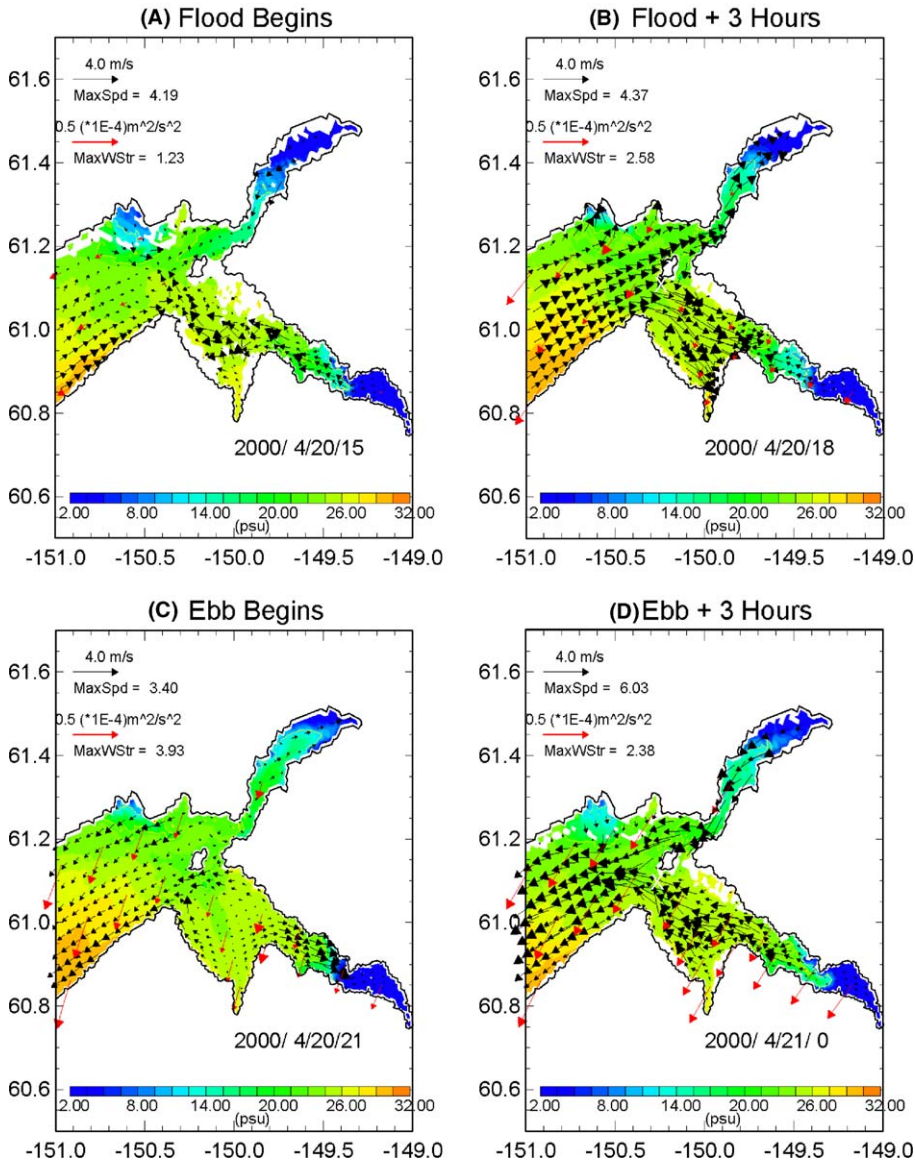

Fig. 13. Simulation of tides and river run-off in Cook Inlet, Gulf of Alaska. Shown here is an enlarged region of the upper inlet where large tidal range exists. Velocity vectors (black) at the first σ-grid nearest the surface are shown superimposed on color images of the corresponding salinity at four different phases of a tidal cycle. Red vectors indicate windstresses used in the model at the indicated dates. Black contour indicates coastline and white regions show dry (and land) areas.

and ebb (panels C and D) phases of the tidal cycle in the upper inlet. Despite the strong buoyancy forcing, variable wind and intense currents, the model has no difficulty simulating wetting and drying. Interesting features include pockets of waters trapped inside topographic 'bowls' during ebb and filling up during flood (cf. O2005).

4. Conclusions

A wetting and drying algorithm for POM in its most general three-dimensional settings with stratification and forcing is presented. The scheme applies to other OGCM's that share POM's features: sigma-coordinate, time-splitting and *C*-grid, and unifies open-ocean models that simulate jets and eddies with coastal-estuarine models that can handle wave run-up (run-down). The new model has been extensively tested (here and also in O2005) and appears to be robust. An application of this kind of open-ocean models with WAD is to forecast hurricane-induced inundations within a unified system that also provides SST information (e.g. of ocean eddies) to hurricane prediction models. An interesting question is how coastal trapped waves (e.g. in storm surge) are modified due to a porous coastal boundary due to WAD. Another is to research effects of wetlands on flood prevention especially under stratified conditions, e.g. near estuarine outflows. If as suggested by this study and O2005 bottom friction is important to inundation physics, future work can couple effects of wind-generated waves and sediment transport into the WAD scheme.

Acknowledgements

I benefited from inputs by Ralph Cheng, Tal Ezer, Shejun Fan, Jeff Ji, Walt Johnson, Dick Prentki and Dong-Ping Wang. Andrey Proshutinsky generously provided the high-resolution topography of the Cook Inlet and Tal Ezer painstakingly charted potential WAD regions. This study is supported by the Minerals Management Service under contract # 0103CT72021. Computing was conducted at GFDL/NOAA.

Appendix A. Two auxiliary WAD implementations for general 3-D flows

The *first* deals with the way WETMASK should be defined so it is consistent in external- and internal-mode integrations. For every N times the external mode is stepped forward, the internal-mode equations are stepped forward once, i.e. $N\Delta t_e = \Delta t_i$. POM averages the external-mode quantities $(\eta, \overline{U}, \overline{V})$ over $N\Delta t_e$ and uses these averages when time-stepping the internal mode (the barotropic pressure gradients for example). It is possible (but rarely, we have found) that a cell can switch from being wet to being dry (and vice versa) during the $N \times \Delta t_e$ external-mode integrations, but it is absurd to define an 'averaged' WETMASK. We therefore set the Nth (i.e. the last) WETMASK from the $N \times \Delta t_e$ external-mode integrations to be the WETMASK used in the internal-mode conditions (2.6) and (2.7).

The *second* concerns boundary conditions in three-dimensional simulations for the shear stress near the bottom (for this subsection only, z measures upward from ocean bottom):

$$K_M\left(\frac{\partial U}{\partial z}, \frac{\partial V}{\partial z}\right) = C_z[U^2 + V^2]^{1/2}(U, V), \quad z \to 0, \tag{A.1}$$

where bottom drag coefficient C_z is obtained by matching the near-bottom modeled velocity to the Law of the Wall (Schlichting, 1968); it is given by:

$$C_z = \mathrm{MAX}\left[\frac{\kappa^2}{[\ln\{z_b/z_0\}]^2}, 0.0025\right], \tag{A.2}$$

where $\kappa = 0.4$ is the von Karman constant, z_0 is the roughness parameter and z_b (>0) is the first velocity grid point nearest (and measured from) the bottom. In (A.1), the eddy viscosity $K_M = |\tau_b/\rho_0|^{1/2}\ell$, where the turbulence length scale ℓ (the Prandtl "mixing length") $= \kappa z$ and τ_b is the bottom stress. Note that the logarithmic Law of the Wall is strictly valid only for sufficiently large z_b/z_0, but not too large ($z_b/z_0 \approx$ 10's–100's). Where the bottom layer is not resolved, for $z_b \approx 3000 z_0$ or larger, (A.2) gives $C_z = 0.0025$. For smooth walls,

$z_0 \approx 0.11\nu/|\tau_b/\rho_0|^{1/2}$ ($\nu \approx 1.14\times10^{-6}$ m^2 s^{-1}) whereas for rough walls $z_0 \approx k_0/30$ where k_0 is the actual wall roughness (Nikuradse, 1933; see Schlichting, 1968, Chapters 19 and 20). The first formula typically gives $z_0 \approx 10^{-4}$ m or less but for rough ocean bottom (second formula) z_0 is typically $> 10^{-3}$ m. Under the influence of waves, an apparent roughness parameter that can be 10–100 times larger than the z_0 in wave-less conditions, may be used (Grant and Madsen, 1979, 1986). During a drying phase of WAD, z_b/z_0 can be $\leqslant 1$ (e.g. 10 cm of water with 10 sigma levels), and the *logarithm* in (A.2) is $\leqslant 0$, which can cause numerical problems. Mellor (2002b) pointed out this dilemma when modeling oscillatory boundary layers for which the apparent roughness parameter was large. He removed near-bottom fine grids to (correctly) avoid the problem, but suggested also modifying the $\ln(z_b/z_0)$ in the Law of the Wall velocity profile by $\ln(1 + z/z_0)$, which asymptotes to $\ln(z/z_0)$ as $z/z_0 \gg 1$, and to z/z_0 (instead of $\leqslant 0$) as z/z_0 becomes small. Thus (A.2) becomes

$$C_z = \mathrm{MAX}\left[\frac{\kappa^2}{[\ln\{1 + z_b/z_0\}]^2}, 0.0025\right], \tag{A.3}$$

and the formula for K_M is changed to $K_M = |\tau_b/\rho_0|^{1/2}(\ell + \kappa z_0)$ leaving the determination of ℓ in Mellor–Yamada turbulence closure scheme unchanged. The 'fix' (A.3) is used in our WAD scheme as a *convenience* to avoid numerical problem related with negative *logarithmic* values (eliminating near-bottom grid points as done by Mellor may be preferred; it would however make the code rife with complicated logic); but the solutions cannot be presumed to be physically correct when z_b/z_0 is small (Mellor, 2002b), as happens near the bottom in cells that are becoming dry or wet.

Appendix B. Formulae for checking conservation properties of tests in text

B.1. Test 1

Volume conservation equation is obtained by integrating the continuity equation (with a source term $q = -w_{\mathrm{River}} \geqslant 0$ on the RHS) over a domain $\mathscr{A}$:

$$\frac{\partial \int\int_{\mathscr{A}} D\,\mathrm{d}x\,\mathrm{d}y}{\partial t} + \oint_{\partial\mathscr{A}} \vec{n}\cdot\vec{\overline{U}}\,\mathrm{d}l = \int\int_{\mathscr{A}} q\,\mathrm{d}x\,\mathrm{d}y, \tag{B.1}$$

where $\vec{n}$ is the unit normal to the boundary $\partial\mathscr{A}$ of $\mathscr{A}$, $\vec{\overline{U}} = (\overline{U}, \overline{V})$. The total (potential + kinetic) energy equation is obtained by adding the domain-A integrals of $\eta\times$continuity equation, $\overline{U}\times x$-momentum equation and $\overline{V}\times y$-momentum equation:

$$\frac{\partial \int\int_{\mathscr{A}} \{g\eta^2 + D(\overline{U}^2 + \overline{V}^2)\}\,\mathrm{d}x\,\mathrm{d}y}{\partial t} + \oint_{\partial\mathscr{A}} \vec{n}\cdot\vec{\overline{U}} D\{2g\eta + \overline{U}^2 + \overline{V}^2\}\,\mathrm{d}l = \int\int_{\mathscr{A}} q\{2g\eta + \overline{U}^2 + \overline{V}^2\}\,\mathrm{d}x\,\mathrm{d}y. \tag{B.2}$$

A dissipation term on the RHS of (B.2) is found to be negligible and is omitted. Note that $\int\int_{\mathscr{A}} \mathrm{d}x\,\mathrm{d}y$ is time-dependent because of WAD even though $\mathscr{A}$ is fixed.

B.2. Test 2

The model solves the following salinity equation written in *sigma-coordinate*:

$$\frac{\partial SD}{\partial t} + \frac{\partial SUD}{\partial x} + \frac{\partial SVD}{\partial y} + \frac{\partial S\omega}{\partial \sigma} = \frac{\partial}{\partial\sigma}\left[\frac{K_H}{D}\frac{\partial S}{\partial\sigma}\right] + F_S, \tag{B.3}$$

where ω is the transformed vertical velocity in σ-space, K_H the vertical eddy diffusivity coefficient and F_S the horizontal diffusion flux. In this case it is easiest to integrate (B.3) over the entire model box bounded by the four walls and $-1 \leqslant \sigma \leqslant 0$ (i.e. from bottom to surface) and noting that either Q or $S = 0$ (i.e. Q inflow with $S = 0$) at $\sigma = 0$ and all fluxes are zero at boundaries (including diffusive flux at the surface):

$$\frac{\partial \int\int\int DS\,\mathrm{d}x\,\mathrm{d}y\,\mathrm{d}\sigma}{\partial t} = 0. \tag{B.4}$$

A box-averaged salinity $\overline{S}(t)$ can be defined so that upon using (B.4) one obtains:

$$\overline{S}(t) = \overline{S}(0)\left[\int\int\int D(0)\,\mathrm{d}x\,\mathrm{d}y\,\mathrm{d}\sigma\right] \Big/ \left[\int\int\int D\,\mathrm{d}x\,\mathrm{d}y\,\mathrm{d}\sigma\right]. \tag{B.5}$$

References

Baines, P.G., 1995. Topographic Effects in Stratified Flows. Cambridge University Press, New York, 482 pp.

Balzano, A., 1998. Evaluation of methods for numerical simulation of wetting and drying in shallow water flow models. Coastal Eng. 34, 83–107.

Blumberg, A.F., Mellor, G.L., 1987. A description of a three-dimensional coastal ocean circulation model. In: Heaps, N. (Ed.), Three-Dimensional Coastal Ocean Models. American Geophysical Union, p. 208.

Casulli, V., Cheng, R., 1992. Semi-implicit finite difference methods for three-dimensional shallow water flow. Int. J. Numer. Methods Fluids 15, 629–648.

Chao, S.-Y., Boicourt, W.C., 1986. Onset of estuarine plumes. J. Phys. Oceanogr. 16, 2137–2149.

Chassignet, E.P., Smith, L.T., Halliwell, G.R., Bleck, R., 2003. North Atlantic simulations with the hybrid coordinate ocean model (HYCOM): impact of the vertical coordinate choice, reference pressure and thermobaricity. J. Phys. Oceanogr. 33, 2504–2526.

Cheng, R.T., Casulli, V., Gartner, J.W., 1993. Tidal, residual, intertidal mudflat (TRIM) model and its application to San Francisco Bay, California. Estuarine, Coastal Shelf Sci. 36, 235–280.

Courant, R., Friedrichs, K.O., Lewy, H., 1928. Uber die partiellen differenzengleichurgen der mathematischen physik. Mathematische Annalen 100, 32–74.

Dinniman, M.S., Klinck, J.M., 2004. A model study of circulation and cross shelf exchange on the west Antarctic Peninsula continental shelf. Deep-Sea Res. II: Top. Stud. Oceanogr. 51, 2003–2022.

Falconer, R.A., Chen, Y., 1991. An improved representation of flooding and drying and wind stress effect in a two-dimensional tidal numerical model. Proc. Inst. Civ. Engrs., Part 2 91 (December), 659–678.

Falconer, R.A., Owens, P.H., 1987. Numerical simulation of flooding and drying in a depth-averaged tidal flow model. Proc. Inst. Civ. Engrs., Part 2 83 (March), 161–180.

Fan, S.J., Oey, L.-Y., Hamilton, P., 2004. Assimilation of drifters and satellite data in a circulation model of the northeastern Gulf of Mexico. Cont. Shelf Res. 24 (9), 1001–1013.

Flather, R.A., Hubbert, K.P., 1990. Tide and surge models for shallow-water-Morecambe Bay revisited. In: Davies, A.M. (Ed.), Modeling Marine Systems, vol. I. CRC Press, pp. 135–166.

Gill, A.E., 1982. Atmosphere–Ocean Dynamics. Academic Press, New York, 662 pp.

Grant, W.D., Madsen, O.S., 1979. Combined wave and current interaction with a rough bottom. J. Geophys. Res. 84, 1797–1808.

Grant, W.D., Madsen, O.S., 1986. The continental-shelf bottom boundary layer. Ann. Rev. Fluid Mech. 18, 265–305.

Hervouet, J.M., Van Haren, L., 1996. Recent advances in numerical methods for fluid flows. In: Anderson, M.G., Walling, D.E., Bates, P.D. (Eds.), Floodplain Processes. Wiley, Chichester, UK, pp. 183–214.

Ji, Z.G., Morton, M.R., Hamrick, J.M., 2001. Wetting and drying simulation of estuarine processes. Estuarine, Coastal Shelf Sci. 53, 683–700.

Ko, D.S., Preller, R.H., Martin, P.J., 2003. An experimental real-time intra Americas sea ocean nowcast/forecast system for coastal prediction. In: Proceedings, AMS 5th Conference on Coastal Atmospheric and Oceanic Prediction and Processes.

LeBlond, P.H., Mysak, L.A., 1978. Waves in the Ocean. Elsevier, Amsterdam.

Leendertse, J.J., 1970. A water-quality simulation model for well-mixed estuaries and coastal seas: principles of computation. Report RM-6230-RC, vol. 1, Rand Corp., Santa Monica, CA, 63 pp.

Lin, B., Falconer, R.A., 1997. Three-dimensional layer-integrated modeling of estuarine flows with flooding and drying. Estuarine Coastal Shelf Sci. 44, 737–751.

Lynch, D.R., Gray, W.G., 1980. Finite-element simulation of flow in deforming regions. J. Comp. Phys. 36, 135–153.

Marchesiello, P., McWilliams, J.C., Shchepetkin, A., 2003. Equilibrium structure and dynamics of the California current system. J. Phys. Oceangr. 33, 753–783.

Mellor, G.L., 2002a. Users' guide for a three-dimensional, primitive equation, numerical ocean model. Program in Atmospheric and Oceanic Sciences, Princeton University, 42pp. Available from: <http://www.aos.princeton.edu/WWWPUBLIC/htdocs.pom>.

Mellor, G.L., 2002b. The oscillatory bottom boundary layer. J. Phys. Oceanogr. 32, 3075–3088.

Nikuradse, J., 1933. Stromungsgesetze in glatten und rauhen rohren. V D I orschungsheft 361, Berlin.

Oey, L.-Y., 1996. Simulation of mesoscale variability in the Gulf of Mexico. J. Phys. Oceanogr. 26, 145–175.

Oey, L.-Y., 2005. A wetting and drying scheme for POM. Ocean Modelling 9, 133–150.

Oey, L.-Y., Chen, P., 1992. A model simulation of circulation in the north-east Atlantic shelves and seas. J. Geophy. Res. 97, 20,087–20,115.

Oey, L.-Y., Mellor, G.L., 1993. Subtidal variability of estuarine outflow, plume and coastal current: a model study. J. Phys. Oceanogr. 23, 164–171.

Oey, L.-Y., Lee, H.-C., Schmitz Jr., W.J., 2003. Effects of winds and caribbean eddies on the frequency of loop current eddy shedding: a numerical model study. J. Geophys. Res. 108 (C10), 3324. doi:10.1029/2002JC001698.

Oey, L.-Y., Winnant, C., Dever, E., Johnson, W., Wang, D.-P., 2004. A model of the near-surface circulation of the Santa Barbara Channel: comparison with observations and dynamical interpretations. J. Phys. Oceangr. 34, 23–43.

Oey, L.-Y., Ezer, T., Forristall, G., Cooper, C., DiMarco, S., Fan, S., 2005. An exercise in forecasting Loop Current and eddy frontal positions in the Gulf of Mexico. Geophys. Res. Lett. 32, L12611. doi:10.1029/2005GL023253.

Romanou, A., Chassignet, E.P., Sturges, W., 2004. The Gulf of Mexico circulation within a high resolution numerical simulation of the North Atlantic Ocean. J. Geophys. Res. 109, CO1003. doi:10.1029/2003CJ001770.

Royer, T.C., 1975. Seasonal variations of waters in the northern Gulf of Alaska. Deep Sea Res. 22, 403–416.

Schlichting, H., 1968. Boundary Layer Theory. McGraw-Hill, New York, 748 pp.

Sheng, J., Tang, L., 2003. A numerical study of circulation in the western Caribbean Sea. J. Phys. Oceanogr. 33, 2049–2069.

Siden, G.L.D., Lynch, D.R., 1988. Wave equation hydrodynamics on deforming elements. Int. J. Numer. Methods Fluids 8, 1071–1093.

Smith, R.D., Maltrud, M.E., Bryan, F.O., Hecht, M.W., 2000. Numerical simulation of the North Atlantic Ocean at 1/10 deg. J. Phys. Oceanogr. 30, 1532–1561.

Smolarkiewicz, P.K., 1984. A fully multidimensional positive definite advection transport algorithm with small implicit diffusion. J. Comput. Phys. 54, 325–362.

Stelling, G.S., Duinmeijer, S.P.A., 2003. A staggered conservative scheme for every Froude number in rapidly varied shallow water flows. Int. J. Numer. Methods Fluids 43, 1329–1354.

Stelling, G.S., Wiersma, A.K., Willemse, J.B.T.M., 1986. Practical aspects of accurate tidal computations. J. ASCE Hydraul. Eng. 9, 802–817.

Titov, V.V., Synolakis, C.E., 1997. Extreme inundation flows during the Hokkaido-Nansei-Oki tsunami. J. Geophys. Lett. 24, 1315–1318.

Xiong, Q., Royer, T.C., 1984. Coastal temperature and salinity in the northern Gulf of Alaska. J. Geophys. Res. 89, 8061–8066.

Ward, S.N., 2001. Tsunamis. In: Meyers, R. (Ed.), Encyclopedia of Physical Science and Technology. Elsevier, Amsterdam, pp. 175–191.

Witham, G.B., 1974. Linear and Nonlinear Waves. Wiley (Interscience), New York.